Linking Glacial-Interglacial states to multiple equilibria of climate

David Ferreira[1], John Marshall[2], Takamitsu Ito[3], David McGee[2]

[1]Department of Meteorology, University of Reading, Reading, UK
[2]Department of Earth, Atmospheric and Planetary Sciences, Massachusetts Institute of Technology, Cambridge, MA, USA
[3]School of Earth and Atmospheric Sciences, Georgia Institute of Technology, Atlanta, USA

Key Points:

- Multiple equilibria of the global climate are found in a coupled ocean-atmosphere-sea ice General Circulation Model
- The two equilibrium states exhibit similarities with the present day climate and that of the Last Glacial Maximum
- The amplitude of the Glacial-Interglacial cycles may be set by such equilibrium states, rather than by the forcing and feedbacks

Corresponding author: David Ferreira, `d.g.ferreira@reading.ac.uk`

Abstract

Glacial-Interglacial cycles are often described as an amplified global response of the climate to perturbations in solar radiation caused by oscillations of Earth's orbit. However, it remains unclear whether internal feedbacks are large enough to account for the radically different Glacial and Interglacial states. Here we provide support for an alternative view: Glacial-Interglacial states are multiple equilibria of the climate system which exist for the same external forcing. We show that such multiple equilibria resembling Glacial and Interglacial states can be found in a complex coupled General Circulation Model of the ocean-atmosphere-sea ice system. The multiple states are sustained by ice-albedo feedback modified by ocean heat transport and are not caused by the bi-stability of the ocean's overturning circulation. In addition, expansion/contraction of the Southern Hemisphere ice pack over regions of upwelling, regulating outgassing of CO_2 to the atmosphere, is the primary mechanism behind a large pCO_2 change between states.

1 Introduction

Over the last 3 million years, Earth's climate has flipped between warm/interglacial conditions, such as the present-day Holocene, and cold/glacial conditions, similar to those found at the Last Glacial Maximum (LGM) 21 kyr ago [*Raymo et al.*, 2006; *Petit and al.*, 1999]. The Glacial-Interglacial cycles (GIC) have been linked to variations of Earth's orbital parameters (Milankovitch cycles), namely precession, obliquity and eccentricity which vary, respectively, with dominant periods of roughly 20, 40 and 100 kyr. However, evidence supporting a link between GIC and Milankovitch cycles is foremost statistical [*Hays et al.*, 1976; *Raymo et al.*, 2006; *Huybers*, 2011]. There is no generally accepted mechanism by which the Milankovitch cycles drive the GIC [*Paillard*, 2015].

A puzzling aspect of the astronomical hypothesis is that small global insolation fluctuations must drive large global shifts of the climate system. This is typically addressed by invoking either strong internal feedbacks or some non-linear mechanism. If strong internal feedbacks are at play, land/sea ice-albedo feedbacks (combined with large local insolation changes) and CO_2 feedbacks are most likely. This behavior has been encapsulated in conceptual models [*Imbrie and Imbrie*, 1980; *Parrenin and Paillard*, 2003], but it remains unclear whether the feedbacks in more realistic models would be large enough to achieve the observed climate shifts in response to the solar forcings. As yet there is no example of a GCM simulating GICs when solely forced with Milankovitch cycles, in the absence of prescribed feedbacks such as land-ice and CO_2 changes.

Taking a non-linear perspective, various studies have explored the possibility of free oscillations of the climate system, paced or phased-locked by the Milankovitch forcing [*Saltzman et al.*, 1984; *Le Treut and Ghil*, 1983; *Gildor and Tziperman*, 2000]. Others hypothesized that Glacial and Interglacial states are two possible equilibrium states of Earth's climate [*Nicolis*, 1982; *Benzi et al.*, 1982; *Paillard*, 1998]. In this case, the Milankovitch radiative forcing provides the "kicks" necessary for the climate system to exceed thresholds and transition between states.

However promising, the latter perspective of the GIC builds on the major assumption that the climate system possesses multiple equilibrium states for a given external forcing. This behavior is commonly found in low-order or conceptual models such as the Budyko-Sellers Energy Balance Model which possess multiple equilibria through sea-ice albedo feedback [*North et al.*, 1981; *Rose and Marshall*, 2009]. However, it is unclear whether more complex systems, and ultimately Earth's climate, can sustain global multiple equilibrium states which resemble Glacial and Interglacial states.

Here, building on previous developments [*Ferreira et al.*, 2011], we first demonstrate that multiple stable states can be sustained in a complex fully dynamical ocean-atmosphere-sea ice General Circulation Model configured with an idealized Earth-like geometry. Second, we show that these equilibrium states exhibit striking similarities to our present-day climate and the climate of the LGM, including signatures on biogeochemical cycles.

2 Modeling context

Simulations are carried out with the MIT GCM [*Marshall et al.*, 1997] which solves for the three-dimensional circulation of atmosphere and ocean, and includes sea ice, and land surface processes. The atmospheric physics is of "intermediate" complexity, based on the simplified parameterizations primitive-equation dynamics (SPEEDY) scheme [*Molteni*, 2003] at low vertical resolution (further details in Text S1). The configuration (Fig. 1) comprises two 45°-wide land masses defining a narrow Atlantic-like basin and a wide Pacific-like basin connecting to an unblocked Southern Ocean (SO). This simplified geometry includes many of the essential dynamics that shape Earth's climate system (e.g. hydrological cycle, storm tracks). It also captures two key asymmetries: an asymmetry between the two Northern basins with the absence of deep water formation in the Pacific [*Ferreira et al.*, 2018] and a North-South asymmetry between a Northern wind-driven gyre regime and a vigorous SO circumpolar current.

In GIC theories, the atmospheric CO_2 changes can be described as a primary driver, a key feedback or an amplifier that can be ignored [see, e.g., *Paillard*, 2015]. Our primary goal here is to demonstrate, in an Earth-like geometry, the possibility of multiple equilibria driven by the dynamical components of the climate system. We focus on the "fast" ocean-atmosphere-sea ice components, neglecting potential feedbacks from, notably, land ice. To facilitate comparison of our results with observations, we also compute the "fingerprints" of the dynamically-driven multiple states on a *passive* carbon cycle model (i.e. one in which CO_2 does not feedback through radiation on the climate state).

Two stable equilibria of climate are supported, one "Cold" and one "Warm" for the same external forcing and parameters, thus demonstrating that multiple equilibria are possible in a coupled GCM comprising a myriad of degrees of freedom. The difference in the climate of the two states is of planetary scale. Global average sea surface temperature and surface air temperature differ by 8.2°C and 13.5°C, respectively [patterns are shown in Fig. S1]. In the Southern Hemisphere (SH), the sea ice edge (as measured by the 15% annual mean concentration) expands by about 15° of latitude in the Cold state (Fig. 1). The Northern Hemisphere, which is nearly ice-free in the Warm state, exhibits a large ice cap extending over the subpolar gyre (45°N) in the Cold state, with a similar expansion of snow cover over land (Fig. 1, top left).

Previous studies of the aquaplanet [*Ferreira et al.*, 2011; *Rose et al.*, 2013; *Rose and Marshall*, 2009; *Rose*, 2015] have revealed that multiple states of the kind shown in Fig. 1 owe their existence to a fundamental and robust feature of the ocean circulation: the ocean heat transport (OHT) peaks near 15-20°N/S and drops sharply in the mid-latitudes (Fig. 2, top right). This reflects the presence on both sides of the Equator of shallow (0-400 m) wind-driven overturning cells associated with the trade winds (Fig. 2) which transport warm surface waters from the Equator into middle latitudes. The pronounced OHT convergence in the subtropics can arrest a runaway expansion of sea ice through the ice-albedo feedback and permits the existence of a steady state with a large ice cap encroaching down into mid-latitudes. Another equilibrium state is possible with nearly ice-free conditions, in which ice albedo feedback promoting the sea ice expansion is weak and easily balanced by the ocean and atmosphere heat transport to the poles. The large ice cap state is unstable in the classic Budyko-Sellers model but stabilized in our GCM by the structure of OHT. This is formalized in a modified Budyko-Sellers-type model [*Rose and Marshall*, 2009; *Ferreira et al.*, 2011] which predicts a stable ice edge on the poleward side of the peak OHT, consistent with our GCM simulations (Fig. 2, top right and Fig. S2).

Previous thinking about the role of multiple equilibrium in past climate changes has been dominated by the idea that the Atlantic meridional overturning circulation (AMOC) possesses bi-stability with an "on" and an "off" state. Abrupt switching between the "on" and "off" modes (triggered by freshwater perturbations) is often invoked to interpret events such as Dansgaard-Oeschger events (*Alley et al.* [2003], but see *Wunsch* [2007] and *Seager and Battisti* [2007] for a critical evaluation). Paleoproxies provide little evidence for a full AMOC collapse at the LGM and rather suggest that a weaker and shallower cell remained active [*Lynch-Stieglitz et al.*, 2007; *Gebbie*, 2014; *Burckel et al.*, 2016]. The AMOC bi-stability is primarily an oceanic process [*Stommel*, 1961]. Signatures of an AMOC collapse are concentrated in the North Atlantic basin with relatively weak (and model dependent) signals outside the Atlantic sector [*Manabe and Stouffer*, 1988; *Vellinga and Wood*, 2002; *Mecking et al.*, 2016]. The multiple states described here differ fundamentally from AMOC bi-stability and are supported by coupled ocean-atmosphere-sea ice dynamics. Although the MOC does change between states in our simulations (Fig. 3), this change does not correspond to a collapse and is in fact a symptom rather than a driver of the bi-stability [*Ferreira et al.*, 2011]. Moreover, the equilibrium states are associated with climate shifts of global extent (Fig. 1) comparable to those observed in the past, providing a novel framework to interpret past climate changes.

3 Circulation patterns in Warm and Cold states

As expected, the Cold state exhibits a weaker hydrological cycle than the Warm state, as illustrated by the smaller amplitude of the evaporation minus precipitation field (Fig. 2), consistent with the "dry gets drier and wet gets wetter" principle seen in global warming experiments [*Held and Soden*, 2006]. The SH jet stream weakens slightly (by $\sim$10%) and shifts northward (by 1.5° lat) in the Cold state, reflecting a northward displacement of the baroclinic zone (strong surface temperature gradient) following the sea ice expansion (further details on the atmospheric states in Text S2 and Fig. S3).

Differences between equilibrium states are also pronounced in the deep ocean. The Cold state has an intensified bottom cell (10 Sv cf 3 Sv of Warm state) emanating from the south (Fig. 3, left). These waters, analogous to Antarctic Bottom Water (AABW) of the present-day ocean, are produced by brine rejection in the regions of production and export of sea ice. As the southern source is stronger in the Cold state, bottom waters approach the freezing point everywhere (~ -1.5°C from 7°C in the Warm state) and become saltier by $\sim$0.5 psu. In contrast, the upper overturning cell (above $\sim$2000 m) is weaker in the Cold state by 5 Sv (Fig. 3). This is not the result of a change in the SH westerly winds and associated upwelling rates. Rather, it is the consequence of a shift in the partitioning of upwelled water between the upper and lower cells: while upwelling mainly feeds the upper cell in the Warm state, upwelled waters are equally partitioned between the upper and lower cells in the Cold state.

The re-organization of the global overturning is consistent with conceptual models highlighting the role of the SH surface buoyancy fluxes in controlling the global MOC, and the depth of the interface between the upper and lower overturning cells [*Ferrari et al.*, 2014; *Watson et al.*, 2015; *Burke et al.*, 2015; *Marzocchi and Jansen*, 2017; *Sun et al.*, 2018]. In steady state, poleward (equatorward) flowing surface waters must lose (gain) buoyancy to (from) the atmosphere and sea ice [*Marshall*, 1997; *Marshall and Radko*, 2003]. Within the ice pack, the ocean experiences net buoyancy loss as freezing and brine rejection dominate exchanges. A transition to net buoyancy gain occurs in the seasonal ice zone, where melting due to exported sea ice dominates. As the sea ice advances in the Cold state, the region of buoyancy loss expands northward (from 70 to 50°S) into the region of wind-driven upwelling, drawing a larger fraction of the upwelled water into the lower cell (Fig. S4). In the adiabatic limit [*Nikurashin and Vallis*, 2012; *Ferrari et al.*, 2014], this sea ice expansion also results in a shoaling of the interface between the two cells, as seen in our simulations (Figs. 3 and S4). In a more realistic GCM including topographically-driven mixing, deep water formation and buoyancy fluxes in the Northern hemisphere may explain about half of the AMOC shoaling [*Sun et al.*, 2018].

In the small (Atlantic-like) basin (Fig. 3, right), the Cold state is associated with a weaker (but non-zero) upper cell (from 20 to 12 Sv), a shoaling of the dense water return flow, a southward shift of deep convection following the ice margin, and a stronger bottom cell fed from the south (see Fig. S5 for the large basin overturning). The large increase in sea ice cover seals off the polar ocean and strongly suppresses air-sea buoyancy flux (see Fig. S4).

Re-organization of the deep circulation between the two states has a profound impact on the distribution of tracers, as illustrated by the phosphate distribution (Fig. 3, right). The nutrient load is dramatically enhanced in the deep ocean of the Cold state relative to the Warm state. While nutrient-depleted waters are only found in the top 300 m in the Warm state, they extend to 2000 m in the Cold state where nutrients accumulate in the bottom cell and remain confined below 2000 m outside of the SO.

4 Atmospheric pCO_2 and biogeochemistry

A fascinating characteristic of the two equilibria is that the atmospheric CO_2 content is significantly lower in the Cold state (157 ppm) than in the Warm state (268 ppm). Both climate states contain the same carbon, phosphate and alkalinity inventories: the atmospheric CO_2 variation is an emergent property of the climate-carbon system resulting from the multiple equilibrium states (but recall that the CO_2 does not feed back on the radiative balance of the atmosphere).

A decomposition of the oceanic carbon reservoir [*Ito and Follows*, 2013] is used to diagnose the relative roles of different carbon pumps in the increased ocean carbon storage in the Cold state (Text S3 for details). This increase is primarily driven by an increased air-sea disequilibrium pump C_{dis} (which measures the ocean carbon storage resulting from an imperfect equilibration between surface waters and the atmospheric pCO_2). This effect is reinforced by an increased solubility pump (due to the cooling between the Warm and Cold states) and is partially compensated by the weakened carbon storage associated with the biological pump (see Table S1 for a summary of the contributions).

In the Warm state, C_{dis} is near neutral (a global mean of +4.3 μmol kg^{-1}) consistent with the modern climatology (Fig. 3, left), where the upper cell is weakly undersaturated ($C_{dis} < 0$) and the lower cell weakly supersaturated ($C_{dis} > 0$). In the Cold state, C_{dis} takes large positive values, indicating a strong supersaturation, equivalent to an atmospheric CO_2 drawdown of -87 ppm (Table S1). The increased C_{dis} is primarily found in the densest water masses confined to the bottom overturning cell (Fig. 3, bottom left). These AABW-like water masses outcrop only in sea-ice covered regions of the SH, which strongly limits the outgassing of CO_2 to the atmosphere. The absence of equilibration between the surface waters and the atmosphere, before the latter are re-injected in the ocean interior, leads to the build up of a large carbon reservoir within the bottom cell. To confirm this interpretation, we carry out a sensitivity experiment in which the capping effect of sea ice on air-sea CO_2 fluxes is removed at latitudes equatorward of the Warm state mean sea ice edge (in the SH only). As a result, the atmospheric CO_2 re-equilibrates at 210 ppm (from 157 ppm) after 4600 years, directly attributing 53 ppm of pCO_2 change to the capping effect of the SH sea ice change between states (the remaining 34 ppm could be due to Northern Hemisphere sea ice effects and changes in residence time of waters at the surface; if anything, temperature effects would contribute a decrease, not an increase, of C_{dis} – see discussions in *Toggweiler et al.* [2003], *Ito and Follows* [2005] and *Ödalen et al.* [2018]).

The glacial storage of CO_2 in the deep ocean by an expansion of the SH sea ice over the upwelling zone was first postulated by *Stephens and Keeling* [2000] using a simple box model in which sea ice cover is prescribed. This idea has been challenged arguing that the seasonal cycle of sea ice cover can expose a significant fraction of the upwelling regions to air-sea equilibration through melting and opening of the sea ice [*Morales Maqueda and Rahmstorf*, 2002; *Sun and Matsumoto*, 2010]. Our calculation explicitly represents the seasonal cycle of sea ice cover and its impact on the air-sea gas transfer as well as its impact on primary production through the availability of light [*Kurahashi-Nakamura et al.*, 2007]. The generation of leads by sea ice dynamics, however, is absent here, although its net effect on CO_2 storage is unclear (as the presence of leads increase air-sea carbon exchanges as well as primary production). Nonetheless, the modeled Warm state successfully reproduces the observed distribution of modern C_{dis} [*Ito and Follows*, 2013]. Our simulations thus lend strong support for such a mechanism provided that the sea ice expansion reaches into the SO upwelling region. It is likely that the reorganization of the MOC also contributes significantly, as a larger fraction of the upwelled water in the SO is transported southward under the Cold state.

It should be noted that our model overestimates the solubility-driven CO_2 drawdown (-58 ppm) because of the large decline in the mean ocean temperature (-7.7°C). For a realistic ocean cooling (2-4°C), we estimate it would be -23±8 ppm, reducing the total CO_2 drawdown to -71±7 ppm (Table S1).

The biological carbon storage is reduced in the Cold state, primarily due to the reorganization of the deep circulation and the dominance of AABW-like water with an elevated preformed phosphorus. In contrast, the surface phosphate is strongly depleted in the ice-free regions of the SH, leading to the decline in the phosphate inventory of the upper overturning cell. The sea ice expansion in the Cold state weakens the biological productivity in the Southern high-latitudes, consistent with paleo-productivity proxies [*Kohfeld et al.*, 2005; *Jaccard et al.*, 2013]. Combining the effects of organic and carbonate pumps (see SI Text S3), the net biological pump increases the atmospheric CO_2 by +36 ppm. When connecting our results to the inferred changes from paleoproxies, the role of the biological carbon pump is the most notable limitation of our study. In particular, our model does not reproduce the elevated glacial productivity in the Subantarctic latitudes, perhaps due to the lack of iron cycling [*Kohfeld et al.*, 2005]. This weakened productivity causes an elevated level of deep water oxygen due to the reduced respiratory O_2 loss, which is inconsistent with bottom water O_2 reconstructions [*Jaccard et al.*, 2009; *Jaccard and Galbraith*, 2011]. The overestimation of ocean cooling also raises the solubility of oxygen, leading to an additional positive bias in the deep O_2 (further discussion of the carbon pumps is found in Text S4).

Despite this limitation, our model reproduces several important features of glacial carbon cycling. Phosphate accumulates in the deep water and is depleted in the upper water column (Fig. 3), consistent with nutrient proxies [*Boyle*, 1988; *Jaccard et al.*, 2009]. While Antarctic preformed nutrient concentrations are relatively high in our model, the deep water still contains a high level of DIC in the lower limb of the MOC due to the elevated level of C_{dis}. This allows the retention of excess DIC in the bottom water while avoiding the widespread anoxia which would occur if the carbon sequestration were dominated by C_{org}.

5 Comparing to the observed Glacial and Interglacial states

Differences between our Warm and Cold states show striking similarities with interglacial and glacial states as inferred from the present climate and that of the LGM, respectively (Fig. 4). Comparison to the present day and LGM is motivated by data availability, and does not imply that all glacial and interglacial states are identical [*Past Interglacials Working Group of PAGES*, 2016]. However, variations among these peak states of the GIC is much smaller than the glacial-interglacial differences which are the focus of our comparison.

Reconstruction of the SO sea ice edge for the LGM indicates a wintertime equatorward displacement between 7 and 10° of latitude relative to present time [*Gersonde et al.*, 2005], which is of the same magnitude as our simulated ice expansion (13° of latitude). Estimates for the summertime LGM are more uncertain but suggest a patchy expansion with large values in the Weddell sector (up to 15° of latitude) and no change in the Indian sector (the sea ice retreating almost back to the coast as today). Our model cannot capture these asymmetries and is likely most relevant to the Weddell sector where the coast is much further south. There, the estimated (15°) and simulated (18°) summertime changes are similar.

Although the strength and position of the SH westerly winds in the glacial periods has received much attention as a possible driver of the atmospheric CO_2 change [*Toggweiler*, 2009], paleoproxy data are very uncertain [*Kohfeld et al.*, 2013; *Shulmeister et al.*, 2004] while simulations of the LGM show very little agreement among models [*Sime et al.*, 2016]. In our simulations, changes in the SH jet stream (Fig. 2) have little impact on CO_2 which is mainly driven by changes in sea ice cover.

In the North Atlantic, paleoproxies suggest that the LGM wintertime sea ice cover was greatly expanded, covering the Nordic Seas and most of the subpolar gyre [*de Vernal et al.*, 2005] and possibly down to the British Isles during stadial conditions [*Dokken et al.*, 2013]. Reconstructions also suggest a southwest-northeast tilted edge along the path of the North Atlantic drift, as seen in our model.

The large shift in deep ocean nutrients between the Warm and Cold states (Fig. 3, left) is consistent with estimates for the present-day and LGM [*Boyle and Keigwin*, 1985]. To help connect with available proxies [*Curry and Oppo*, 2005; *Peterson et al.*, 2014], estimates of the equivalent $\delta^{13}C$ distributions for the two states are shown in Fig. S6. Notwithstanding limitations due to the idealized geometry, the two states capture important large-scale changes seen in observations, notably the near doubling of the top-to-bottom $\delta^{13}C$ gradient at the LGM [*Curry and Oppo*, 2005; *Peterson et al.*, 2014]. These rearrangements of the tracer distributions (e.g. $\delta^{13}C$) have been interpreted as reflecting a slightly weaker and shallower AMOC at the LGM [*Curry and Oppo*, 2005; *Lynch-Stieglitz et al.*, 2007; *Peterson et al.*, 2014]. Although such interpretations should be taken with caution [*Gebbie*, 2014], we do observe a consistent set of changes in circulation/tracer patterns that parallels those inferred for the LGM.

Bottom waters at the LGM are estimated to be near the freezing point at all latitudes and saltier than today by 1 and 2.4 psu [*Adkins et al.*, 2002]. Similar tendencies are seen in our simulations although bottom salinity only increases by +0.5 psu in the SO, decreasing to zero at the North pole. As our model does not allow large accumulation of freshwater over land (we do not have ice sheets), the modeled salinity shifts provides an estimate of the contribution of ocean circulation changes and increased brine rejection to the observed change.

It is apparent that the temperature difference between the two states is larger than inferred for the LGM-present difference. This is traceable to a warm bias in Northern surface temperatures of the Warm state which is communicated to the global ocean through deep water formation (at ∼7°C compared to ∼3°C for the present day). This could be due to our idealized land distribution that facilitates OHT toward high latitudes, and/or the narrow width of the continent that limits the advection of cold dry air over the oceans.

6 Conclusions

We have shown that multiple equilibria of global scale are possible in a complex coupled GCM with an Earth-like geometry. The robust dynamics that enables such states (a large heat release from the ocean to the atmosphere in mid-latitudes [*Rose and Marshall*, 2009; *Ferreira et al.*, 2011]) suggests that they could exist in Earth's climate. Important similarities (both in terms of circulation and biogeochemical signatures) between our two climate states and that of the LGM/present-day suggest that GIC could be sustained by the existence of multiple equilibria. If confirmed, this would have a profound impact on our interpretation of the paleo-record, notably of the relationship between the Milankovitch cycles and the observed response.

Importantly, such a link does not imply that all glacial and interglacial states should be identical. Internal noise in the climate system (e.g. millennial AMOC variability), changes in the internal feedbacks (e.g. land ice, CO_2) and changes in the Milankovitch cycles could perturb trajectories through the "potential wells" of the multiple states. In fact, a more pressing question is why the GIC's amplitude is so regular considering the highly variable magnitudes of insolation change during glacial terminations [*Petit and al.*, 1999].

Linking the GIC to multiple stables states can provide an answer as in such case the GIC's amplitude is primarily determined by the separation between the multiple states (a property of the unperturbed system) rather than by the forcing. The latter then provides the "kicks" to trigger the transition from one potential well to the other. Paillard's conceptual model illustrates these properties [*Paillard*, 1998]: when driven by Milankovitch cycles, the magnitude of the cycles is relatively stable (compared to the variability in the forcing) but also allows for differences in the peak value and duration of the interglacials (see his Fig. 4).

Our main goal here has been to reveal the possibility of multiple states sustained by the dynamical components of the climate system, and to put forward a novel perspective on the dynamics of GIC. Although our study represents a large step forward from the conceptual/analytical models used previously [e.g. *Paillard*, 1998; *Benzi et al.*, 1982], critical issues remain to be addressed to advance this view. Future work should test whether these states persist in the presence of improved physics, notably land ice and radiative CO_2 feedbacks. Ice sheet dynamics are often proposed as an essential element of GIC dynamics [*Imbrie and Imbrie*, 1980; *Paillard*, 1998; *Abe-Ouchi et al.*, 2013; *Muglia and Schmittner*, 2015], possibly responsible for the asymmetry between the fast deglaciations and the slower inceptions. The absence of a radiative CO_2 feedback in our experiments is also a major limitation as such a positive feedback may destabilize the multiple states. A simple sensitivity experiment in which a radiative perturbation of about -3 W m^2 (equivalent to a $\sim$100 ppm pCO_2 drop) is imposed in the Cold state shows that this state remains stable although it is driven farther apart from the Warm state (not shown). As pointed out above, the separation between the states (in, say, global temperature) is most likely influenced by the highly idealized continental geometry employed here. Further evaluation of the multiple states, notably their similarity with Glacial/Interglacial states, will require use of a more realistic geometry. This is also essential to permit closer a comparison with available proxies.

The ideas presented here need to be tested in more complex GCMs. We feel that the search for such equilibria in climate models has been neglected and should be more systematic, as was done for example for the bi-stability of the overturning circulation.

Acknowledgments

JM would like to acknowledge support from NSF and NOAA. Data supporting the results reported in this paper are openly available from the University of Reading Research Data Archive at http://dx.doi.org/10.17864/1947.156.

References

Abe-Ouchi, A., F. Saito, K. Kawamura, M. E. Raymo, J. Okuno, K. Takahashi, and H. Blatter (2013), Insolation-driven 100,000-year glacial cycles and hysteresis of ice-sheet volume, *Nature*, *500*, 190–194.

Adkins, J. F., K. McIntyre, and D. Schrag (2002), The salinity, temperature and δ^{18}O of the glacial deep ocean, *Science*, *298*, 1769–1773.

Alley, R., J. Marotzke, W. D. Nordhaus, J. T. Overpeck, D. M. Peteet, R. A. Pielke Jr, R. T. Pierrehumbert, P. B. Rhines, T. F. Stocker, L. D. Talley, and J. M. Wallace (2003), Abrupt climate change, *Science*, (29), 2005–2010.

Benzi, R., G. Parisi, A. Sutera, and A. Vulpiani (1982), Stochastic resonance in climatic change, *Tellus*, *34*, 10–16.

Boyle, E. A. (1988), Vertical oceanic nutrient fractionation and glacial/interglacial co2 cycles, *Nature*, *331*, 55–56.

Boyle, E. A., and L. D. Keigwin (1985), Comparison of atlantic and pacific paleochemical records for the last 215,000 years: changes in deep ocean circulation and chemical inventories, *Earth and Planet. Sci. Lett.*, *76*, 135–150.

Burckel, P., C. Waelbroeck, Y. Luo, D. M. Roche, S. Pichat, S. L. Jaccard, J. Gherardi, A. Govin, J. Lippold, and F. Thil (2016), Changes in the geometry and strength of the atlantic meridional overturning circulation during the last glacial (20–50 ka), *Clim. Past*, *12*, 2061–2075.

Burke, A., A. L. Stewart, J. F. Adkins, R. Ferrari, M. F. Jansen, and A. F. Thompson (2015), The glacial mid-depth radiocarbon bulge and its implications for the over- turning circulation, *Paleoceanography*, *30*, 1021–1039.

Curry, W. B., and D. W. Oppo (2005), Glacial water mass geometry and the distribution of δ^{13}C of CO_2 in the western atlantic ocean, *Paleoceanography*, *24*, PA1017.

de Vernal, A., F. Eynaud, M. Henry, C. Hillaire-Marcel, L. Londeix, S. Mangin, J. Matthiessen, F. Marret, T. Radi, A. Rochon, S. Solignac, and J.-L. Turon

(2005), Reconstruction of sea-surface conditions at middle to high latitudes of the northern hemisphere during the last glacial maximum (LGM) based on dinoflagellate cyst assemblages, *Quat. Sci. Rev.*, *24*, 897–924.

Dokken, T., K. H. Nisancioglu, C. Li, and D. Battisti (2013), Dansgaard-oeschger cycles: Interactions between ocean and sea ice intrinsic to the nordic seas, *Paleoceanography*, *28*, 491–502.

Ferrari, R., M. J. Jansen, J. F. Adkins, A. Butke, A. L. Stewart, and A. F. Thompson (2014), Antarctic sea ice control on ocean circulation in present and glacial climates, *Proc. Natl. Acad. Sci.*, *111*(24), 8753–8758.

Ferreira, D., J. Marshall, and B. Rose (2011), Climate determinism revisited: multiple equilibria in a complex climate model, *J. Climate*, *24*, 992–1012.

Ferreira, D., P. Cessi, H. K. Coxall, A. de Boer, H. A. Dijkstra, S. S. Drijfhout, T. Eldevik, N. Harnik, J. F. McManus, D. P. Marshall, J. Nilsson, F. Roquet, T. Schneider, and R. C. Wills (2018), Atlantic-pacific asymmetry in deep-water formation, *Annu. Rev. Earth Planet. Sci.*, *46*.

Gebbie, G. (2014), How much did glacial north atlantic water shoal?, *Paleoceanography*, *29*(3), 190–209.

Gersonde, R., X. Crosta, A. Abelmann, and L. Armand (2005), Sea-surface temperature and sea ice distribution of the southern ocean at the epilog last glacial maximum—a circum-antarctic view based on siliceous microfossil records, *Quat. Sci. Rev.*, *24*, 869–896.

Gildor, H., and E. Tziperman (2000), Sea ice as the galical cycles's climate switch: Role of seasonal and orbital forcing, *Paleoceanography*, *15*, 605–615.

Hays, J. D., J. Imbrie, and N. J. Shackleton (1976), Variations in the earth's orbit: Pacemaker of the ice ages, *Science*, *194*(4270), 1121–1132.

Held, I., and B. J. Soden (2006), Robust responses of the hydrological cycle to global warming, *J. Climate*, *19*, 5686–5699.

Huybers, P. (2011), Combined obliquity and precession pacing of late pleistocene deglaciations, *Nature*, *480*, 229–232.

Imbrie, J., and J. Z. Imbrie (1980), Modeling the climatic response to orbital variations, *Science*, *207*(4434), 943–953.

Ito, T., and M. J. Follows (2005), Preformed phosphate, soft tissue pump and atmospheric CO_2, *J. Mar. Res.*, *63*, 813–839.

Ito, T., and M. J. Follows (2013), Air-sea disequilibrium of carbon dioxide enhances the biological carbon sequestration in the southern ocean, *Glob. Biogeochem. Cy.*, *27*, 1–10.

Jaccard, S. L., and E. D. Galbraith (2011), Large climate-driven changes of oceanic oxygen concentrations during the last deglaciation, *Nature Geoscience*, *5*, 151–156.

Jaccard, S. L., E. D. Galbraith, D. M. Sigman, G. H. Haugh, R. F. Francois, T. F. Petersen, P. Dulski, and H. R. Thierstein (2009), Subarctic pacific evidence for a glacial deepening of the oceanic respired carbon pool, *Earth and Planet. Sci. Lett.*, *277*, 156–165.

Jaccard, S. L., C. T. Hayes, A. Martinez-Garcia, D. A. Hodell, R. F. Anderson, D. M. Sigman, and G. H. Haugh (2013), Two modes of change in southern ocean productivity over the past million years, *Science*, *339*, 1419–1423.

Kohfeld, K. E., C. Le Quéré, S. P. Harrison, and R. F. Anderson (2005), Role of marine biology in glacial-interglacial co2 cycles, *Science*, *308*, 74–78.

Kohfeld, K. E., R. M. Graham, A. M. de Boer, L. C. Sime, E. W. Wolff, C. Le Quéré, and L. Bopp (2013), Southern hemisphere westerly wind changes during the last glacial maximum: paleo-data synthesis, *Quat. Sci. Rev.*, *68*, 76–95.

Kurahashi-Nakamura, T., A. Abe-Ouchi, Y. Yamanaka, and K. Misumi (2007), Compound effects of antarctic sea ice on atmospheric pco2 change during glacial–interglacial cycle, *Geophys. Res. Lett.*, *34*(L20708).

Le Treut, H., and M. Ghil (1983), Orbital forcing, climatic interactions, and glaciation cycles, *J. Geophys. Res.*, *88*(C9), 5167–5190.

Lynch-Stieglitz, J., J. F. Adkins, W. B. Curry, T. Dokken, I. R. Hall, J. C. Herguera, J. J.-M. Hirshi, E. V. Ivanova, C. Kissel, O. Marchal, T. M. Marchitto, I. N. McCave, J. F. McManus, S. Mulitza, U. Ninnemann, F. Peeters, E.-F. Yu, and R. Zahn (2007), Atlantic meridional overturning circulation during the last glacial maximum, *Science*, *316*, 66–69.

Manabe, S., and R. J. Stouffer (1988), Two stable equilibria of a coupled ocean-atmosphere model, *J. Climate*, *1*, 841–866.

Marshall, D. (1997), Subduction of water masses in an eddying ocean, *J. Mar. Res.*, *55*(2), 201–222.

Marshall, J., and T. Radko (2003), Residual mean solutions for the antarctic circumpolar current and its associated overturning circulation, *J. Phys. Oceanogr.*, *33*, 2341–2354.

Marshall, J., A. Adcroft, C. Hill, L. Perelman, and C. Heisey (1997), A finite-volume, incompressible navier stokes model for studies of the ocean on parallel computers, *J. Geophys. Res.*, *102*(C3), 5753–5766.

Marzocchi, A., and M. F. Jansen (2017), Connecting antarctic sea ice to deep-ocean circulation in modern and glacial climate simulations, *Geophys. Res. Lett.*, *44*.

Mecking, J. V., S. S. Drijfhout, L. C. Jackson, and T. Graham (2016), Stable amoc off state in an eddypermitting coupled climate model, *Climate Dyn.*, *47*, 2455–2470.

Molteni, F. (2003), Atmospheric simulations using a GCM with simplified physical parametrizations. I: model climatology and variability in multi-decadal experiments., *Climate Dyn.*, *64*, 175–191.

Morales Maqueda, M. A., and S. Rahmstorf (2002), Did antarctic sea-ice expansion cause glacial CO_2 decline?, *Geophys. Res. Lett.*, *29*, 1011.

Muglia, J., and A. Schmittner (2015), Glacial atlantic over- turning increased by wind stress in climate models, *Geophys. Res. Lett.*, *42*, 9862–9869.

Nicolis, C. (1982), Stochastic aspects of climatic transitions – response to a periodic forcing, *Tellus*, *34*, 1–9.

Nikurashin, M., and G. K. Vallis (2012), A theory of the interhemispheric meridional overturning circulation and associated stratification, *J. Phys. Oceanogr.*, *42*(10), 1652–1667.

North, G. R., R. F. Cahalan, and J. A. C. Jr (1981), Energy balance climate models, *Rev. Geophysics and Space Physics*, *19*, 91–121.

Ödalen, M., J. Nycander, K. I. C. Oliver, L. Brodeau, and A. Ridgwell (2018), The influence of the ocean circulation state on ocean carbon storage and CO_2 drawdown potential in an earth system model, *Biogeosciences*, *15*, 1367–1393, doi:10.5194/bg-15-1367-2018.

Paillard, D. (1998), The timing of pleistocene glaciations from a simple multiple-state climate model, *Nature*, *391*, 378–381.

Paillard, D. (2015), Quaternary glaciations: from observations to theories, *Quat. Sci. Rev.*, *107*, 11–24.

Parrenin, F., and D. Paillard (2003), Amplitude and phase of glacial cycles from a conceptual model, *Earth and Planet. Sci. Lett.*, *214*, 243–250.

Past Interglacials Working Group of PAGES (2016), Interglacials of the last 800,000years, *Rev. Geophys.*, *54*.

Peterson, C. D., L. E. Lisiecki, and J. V. Stern (2014), Deglacial whole-ocean δ^{13}c change estimated from 480 benthic foraminiferal records, *Paleoceanography*, *29*, 549–563.

Petit, J. R., and al. (1999), Climate and atmospheric history of the past 420,000 years from the vostok ice core, Antarctica, *Nature*, *399*, 429–436.

Raymo, M. E., L. E. Lisiecki, and K. H. Nisancioglu (2006), Plio-pleistocene ice volume, Antarctic climate, and the global δ^{18}O record, *Science*, *313*, 492–495.

Rose, B. (2015), Stable "water- belt" climates controlled by tropical ocean heat transport: A nonlin- ear coupled climate mechanism of relevance to snowball earth, *J. Geophys. Res.*, *120*, 1404–1423.

Rose, B., D. Ferreira, and J. Marshall (2013), The role of oceans and sea ice in abrupt transitions between multiple climate states, *J. Climate*, *26*, 2862–2879.

Rose, B. E., and J. Marshall (2009), Ocean Heat Transport, sea ice and multiple climatic states: Insights from Energy Balance Models, *J. Atmos. Sci.*, *66*, 2828–2843.

Saltzman, B., A. R. Hansen, and K. A. Maasch (1984), The late quaternary glaciatiosn as the response of a three-component feedback system to the earth-orbital forcing, *J. Atmos. Sci.*, *41*(23), 3380–3389.

Seager, R., and D. S. Battisti (2007), *The Global Circulation of the Atmosphere*, chap. Challenges to Our Understanding of the General Circulation: Abrupt Climate Change, Princeton University Press.

Shulmeister, J., G. Goodwin, J. Renwick, K. Harle, L. Armand, M. S. McGlone, E. Cook, J. Dodson, P. P. Hesse, P. Mayewski, and M. Curran (2004), The southern hemisphere westerlies in the australasian sector over the last glacial cycle: a synthesis, *Quat. Int.*, *118*, 23–53.

Sime, L. C., D. Hodgson, T. J. Bracegirdle, C. Allen, B. Perren, S. Roberts, and A. M. de Boer (2016), Sea ice led to poleward-shifted winds at the last glacial maximum: the influence of state dependency on CMIP5 and PMIP3 models, *Clim. Past Discuss.*, *12*, 2241–2253.

Stephens, B. B., and R. F. Keeling (2000), The influence of antarctic sea ice on glacial-interglacial CO_2 variations, *Nature*, *404*, 171–174.

Stommel, H. (1961), Thermohaline convection with two stable regimes of flow, *Tellus*, *13*(2), 224–230.

Sun, S., I. Eisenman, and A. Stewart (2018), Does southern ocean surface forcing shape the global ocean overturning circulation?, *Geophys. Res. Lett.*, *45*.

Sun, X., and K. Matsumoto (2010), Effects of sea ice on atmospheric pCO_2: A revised view and implications for glacial and future climates, *J. Geophys. Res.*, *115*, G02,015.

Toggweiler, J. R. (2009), Shifting westerlies, *Science*, *323*, 1434–1435.

Toggweiler, J. R., A. Gnanadesikan, S. Carson, R. Murnane, and J. L. Sarmiento (2003), Representation of the carbon cycle in box models and gcms: 1. solubility pump, *Glob. Biogeochem. Cy.*, *17*, 1026, doi:10.1029/2001GB001401.

Vellinga, M., and R. Wood (2002), Global climatic impacts of a collapse of the atlantic thermohaline circulation, *Climate Change*, *54*, 251–267.

Watson, A. J., G. K. Vallis, and M. Nikurashin (2015), Southern ocean buoyancy forcing of ocean ventilation and glacial atmospheric CO_2, *Nature Geoscience*, *8*, 861–864.

Wunsch, C. (2007), *Ocean Circulation: Mechanisms and Impacts - Past and Future Changes of Meridional Overturning*, chap. The past and future ocean circulation from a contemporary perspective, American Geophysical Union, Washington, DC.

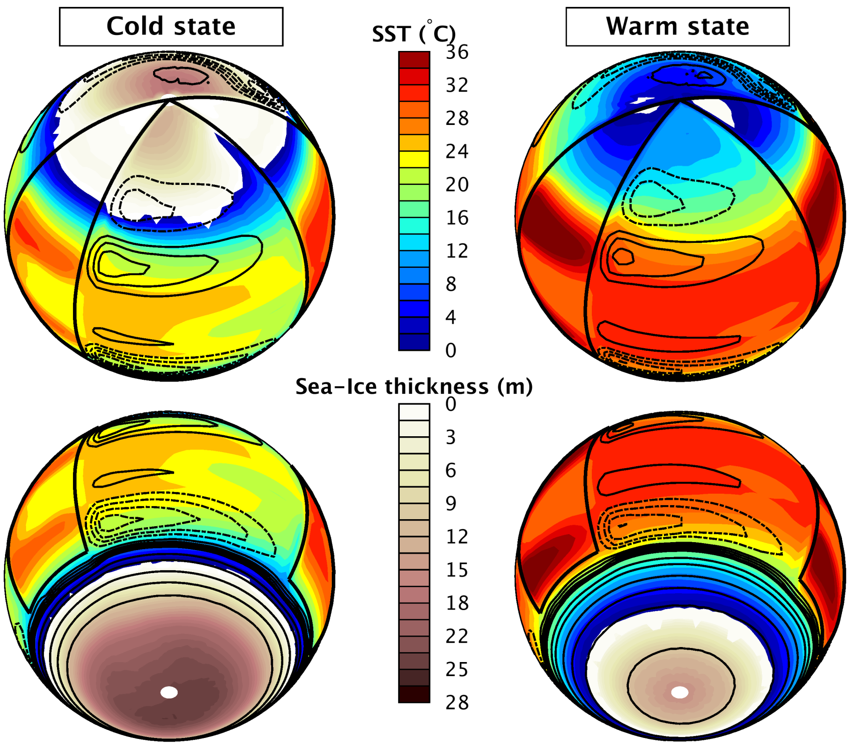

Figure 1. Temperature and ice distributions in the two equilibrium states. Sea Surface Temperature (blue-red shading, in °C) and sea ice thickness (white-brown shading, in meter) for the (left) Cold and (right) Warm states. Over the continents, the Surface Air Temperature and snow depth are shown instead. The thick solid line denotes the continental boundaries. The barotropic streamfunction for the ocean is shown in black contours (solid for clockwise, dashed for counter clockwise). Both states are obtained for the same external forcing and same parameters.

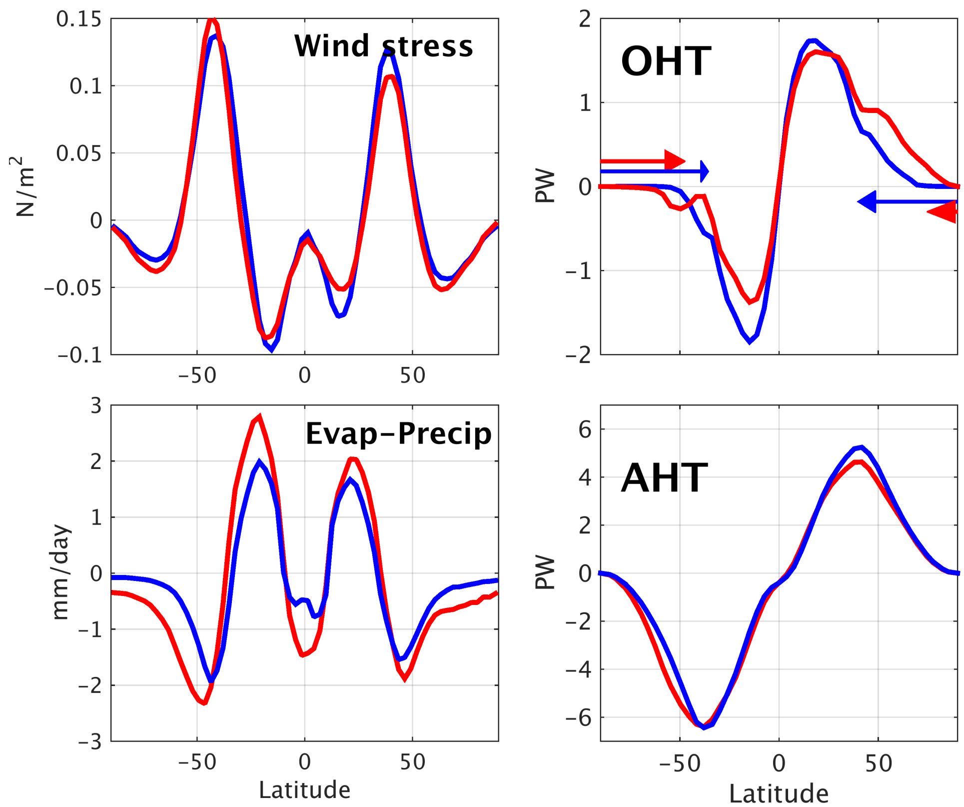

Figure 2. Surface zonal wind stress (N/m^2, top left), evaporation minus precipitation (mm/day, bottom left) and the net energy transports (in PW $=10^{15}$ W) in the ocean (top right) and atmosphere (bottom, right). The Warm and Cold states are denoted by red and blue lines, respectively. Horizontal arrows indicate the sea ice extent (15% sea ice fraction) where the length of the arrowheads denote the minimum/maximum seasonal range.

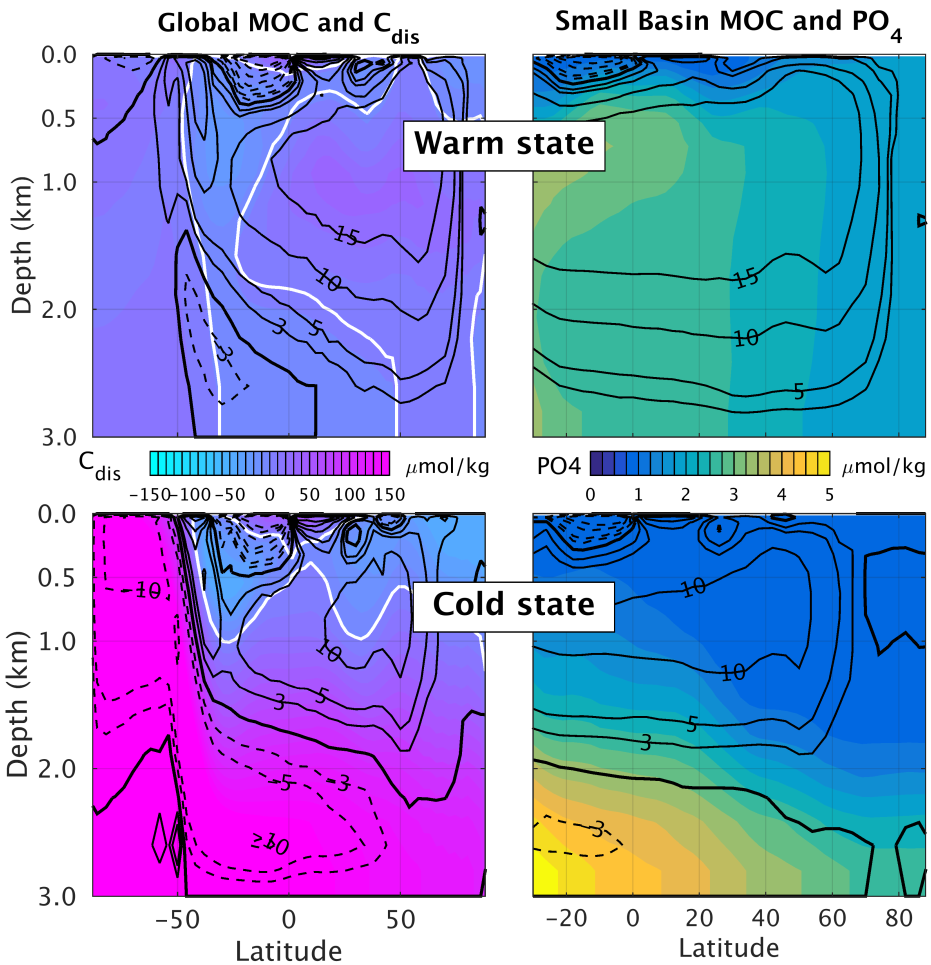

Figure 3. (Left) Global overturning circulation (in Sv, black lines) overlaid on the global disequilibrium reservoir C_{dis} (shading, in μmol/kg; zero contour highlighted with a thick white line). (Right) small basin overturning circulation overlaid on phosphate concentration (in μmol kg^{-1}). For the overturning, solid and dashed lines denote clockwise and counter-clockwise circulations, respectively. The Warm state is shown in the top row and the Cold state in the bottom row.

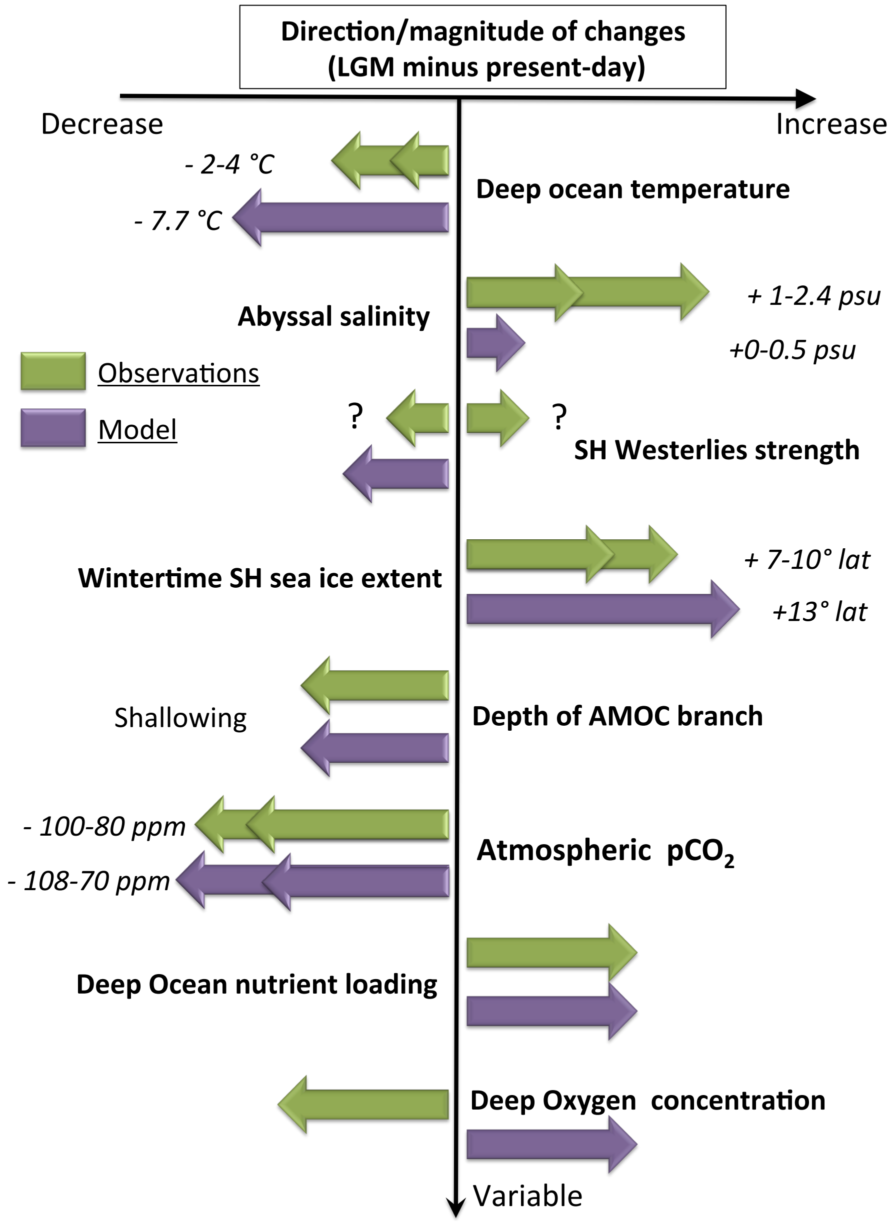

Figure 4. Observed changes between the LGM and present-day climates from observations (green arrows) along with the corresponding differences between the Cold and Warm states of our idealized Earth-like climate simulations (purple arrows). When possible, arrows are scaled to represent the magnitude of the changes. Double arrows indicate the range of uncertainties.

Supporting Information for "Linking Glacial-Interglacial states to multiple equilibria of climate"

David Ferreira,[1] John Marshall,[2] Takamitsu Ito,[3] David McGee[2]

[1]Department of Meteorology, University of Reading, Reading, UK.

[2]Department of Earth, Atmospheric and Planetary Sciences, Massachusetts Institute of Technology, Cambridge, MA, USA.

[3]School of Earth and Atmospheric Sciences, Georgia Institute of Technology, Atlanta, USA.

Contents

1. Text S1 to S4
2. Table S1
3. Figures S1 to S6

Text S1. Climate modelling framework

We use the Massachusetts Institute of Technology (MIT) GCM in a coupled ocean-atmosphere-sea ice setup [*Marshall et al.*, 1997a,b]. The model exploits an isomorphism between the ocean and atmosphere dynamics to generate an atmospheric GCM and an oceanic GCM from the same dynamic core [*Marshall et al.*, 2004]. The model uses the following (isomorphic) vertical coordinates: the rescaled pressure coordinate $p^\star$ for the compressible atmosphere and the rescaled height coordinate $z^\star$ for the Boussinesq ocean [*Adcroft and Campin*, 2004]. Both component models use the same cubed-sphere grid [*Adcroft et al.*, 2004], at a low-resolution C24 (24×24 points per face, yielding a resolution of 3.75° at the equator). The cubed-sphere grid avoids problems associated with the converging meridian at the poles and ensures that the model dynamics at the poles are treated with as much fidelity as elsewhere. Additionally, it greatly simplifies the implementation of a conservative interface between the two GCMs [*Campin et al.*, 2008].

The atmospheric physics is of "intermediate" complexity, based on the simplified parameterizations primitive-equation dynamics (SPEEDY) scheme [*Molteni*, 2003] at low vertical resolution (five levels). This method comprises a four-band radiation scheme,

Corresponding author: David Ferreira, `d.g.ferreira@reading.ac.uk`

a parameterization of moist convection, diagnostic clouds, and a boundary layer scheme. The 3 km-deep, flat-bottomed ocean model has 15 vertical levels, increasing from 30 m at the surface to 400 m at depth. Effects of mesoscale eddies are parameterized as an advective process [*Gent and McWilliams*, 1990] and an isopycnal diffusion [*Redi*, 1982], both with a transfer coefficient of 1200 m^2 s^{-1}. Convective adjustment, implemented as an enhanced vertical mixing of temperature and salinity, is used to represent ocean convection [*Klinger et al.*, 1996]. The background vertical diffusion is uniform and set to $3{\times}10^{-5}$ m^2 s^{-1}. The sea ice model uses a two-and-a-half-layer thermodynamic formulation following *Winton* [2000]. The prognostic variables are ice fraction, snow and ice thickness, and a two-level enthalpy representation accounting for brine pockets and sea ice salinity employes an energy-conserving formulation. There are no sea ice dynamics. The land model is a simple two-layer model with prognostic temperature, liquid groundwater, and snow height. There is no continental ice. The land albedo is to set to 0.10 plus a contribution from snow, if present. The snow albedo parameterization (identical over land and sea ice) depends on the snow height, surface temperature, and snow age. Present-day orbital forcing is used and pCO_2 is set to 325 ppm in the radiative scheme. The seasonal cycle is represented but there is no diurnal cycle.

The biogeochemical component of the model consists of five tracers including Dissolved Inorganic Carbon (DIC), alkalinity, phosphate, dissolved organic phosphorus and oxygen [*Dutkiewicz et al.*, 2006]. The rates of carbon uptake and oxygen production are calculated based on the availability of phosphate and light using the Monod function. 67% of phosphate uptake turns into dissolved organic matter, and the remaining 33% sinks down as particulate organic matter. A Martin exponent of 0.90 is used for the parameterization of the vertical attenuation of sinking particles, and the dissolved organic matter decays back to inorganic nutrient and carbon with the e-folding time scale of 6 months. Remineralization of sinking organic matter and dissolved organic matter consumes oxygen with a globally uniform stoichiometric ratio, $P{:}C{:}O_2$ = 1:110:170. The oceanic carbon cycle is coupled to a well-mixed atmospheric reservoir of CO_2. The atmospheric CO_2 is not active radiatively active, however, and so the carbon cycle does not feed back on climate dynamics. Our focus here is on the existence of multiple states supported by the coupled dynamics, and we choose to initially treat the biogeochemical cycles as a passive component.

Finally, fluxes of momentum, freshwater, heat, salt and CO_2 are exchanged every hour (the ocean time step). Note that the present coupled ocean-sea ice-atmosphere model achieves perfect (machine accuracy) conservation of freshwater, heat, and salt during extended climate simulations [*Campin et al.*, 2008]. This is made possible by the use of the $z^\star$ coordinate, which allows for a realistic treatment of the sea ice-ocean interface. This property is crucial to the fidelity and integrity of the coupled system.The model (or close versions of it) has been used before in process studies [*Marshall et al.*, 2007; *Ferreira et al.*, 2010, 2011] with idealized configurations as well as realistic paleoclimate configurations [*Pohl et al.*, 2017].

Initial conditions for the two states. The two simulations were started from different initial conditions. The Warm state was initialized from the zonal mean state of the "Double-Drake" simulation [*Ferreira et al.*, 2010] which has an ice cover at the Southern pole but not at the Northern pole. Initial conditions for the Cold state were obtained as follows: the model was again started from the zonal mean state of the "Double-Drake" simulation but with a higher value of the ground albedo of 0.25 (typical of a rocky/desert conditions) everywhere over the continents. This albedo choice drives a global cooling of the climate system and the growth of extensive ice caps at both poles. The equilibrium state of this simulation is used as cold initial conditions to start a simulation with the exact same parameters and forcing as the Warm state (including the same ground albedo). This simulation remains in a cold climate, hence producing a second equilibrium state (the Cold state). Both the Warm and Cold solutions have been run up to equilibrium.

Text S2. Oceanic and atmospheric energy transports

As expected from previous studies [*Stone*, 1978; *Enderton and Marshall*, 2009], the total (ocean plus atmosphere) energy transport remains relatively similar between the two states, notably over regions unaffected by changes in the sea ice cover (Fig. S2, bottom). This invariance provides an interesting constraint to interpret the ocean and atmospheric energy transports.

As the Ocean Heat Transport (OHT) in the deep tropics varies little between the two states (Fig. 2, top right), the Atmospheric Heat Transport (AHT) must also remains similar. As the moist static energy contrast between the top and bottom of the troposphere is weaker in the Cold state (lower specific humidity), an intensification of the Hadley circulation in the Cold state is required to maintain the strength of the AHT at low latitudes (Fig. S3).

It is also noteworthy that the invariance of the total heat transport hides a number of compensating changes in ocean and atmospheric transports. Within the AHT, the decrease of the latent heat transport in the Cold state is largely balanced by an increase of the dry static component (not shown). Exceptions to this are found in regions of the sea ice cover change. In the band 70-50°S (ice free in the Warm state), the equatorward displacement of the storm track (with the sea ice expansion) and cooling in the Cold state result in decreases of both latent and dry static energy transports. In the northern hemisphere, in contrast, the strengthening of the storm tracks (without displacement) is associated with an intensification of the dry static energy transport which is only partially cancelled by a decreased latent heat transport.

In the ocean, the OHT undergoes a reorganization associated with changes in the deep circulation, sea-ice cover, and winds. In the Northern Hemisphere, the OHT of the small (Atlantic-like) basin decreases at all latitudes by ∼0.4 PW in the Cold state (Fig. S2, top), reflecting the weakening of the deep MOC. In the large basin however, the OHT in the band 0-30°N intensifies (by about 0.5 PW) in response to the strengthening of the Hadley Cell/Trade winds (i.e. strengthening of the wind-driven component of the circulation). As a results, the global OHT in the subtropics is slightly larger in the Cold state than in the Warm state (Fig. 2, top right). North of 40°N, the weakened deep MOC dominates the global OHT change which exhibits a decrease in the Cold state.

Change in the strength of the bottom cell has little impact on the OHT (the bottom cell acts on weak vertical temperature gradient and achieves little heat transport; see [*Ferrari and Ferreira*, 2011]). The OHT change in the Southern Hemisphere (0-40°S) is dominated by the weakening of upper deep cell (which transports heat northward, leading to a stronger southward transport in the Cold state, see Fig. 2). South of 40°S, changes in OHT primarily reflect the expansion of the sea ice cover that strongly damps air-sea exchanges.

Text S3. Carbon pump analysis

Changes in the equilibrium atmospheric CO_2 (δpCO_2) can be attributed to changes in oceanic carbon reservoirs and the total carbon inventory of the ocean-atmosphere system [*Ito and Follows*, 2005, 2013]:

$$\delta pCO_2 = \left(M + \frac{V\overline{C_{ref}}}{pCO_{2,ref}B} \right)^{-1} \left(\delta I_C - V\delta\overline{C} \right), \qquad (1)$$

where M is the total moles of gases in the atmosphere, V is the volume of the ocean, B is the global mean Buffer factor (set to 12 in this study), and I_C is the total carbon inventory of the ocean-atmosphere system. The overline indicates the global mean. In the closed system ($\delta I_C = 0$) the change of atmospheric CO_2 is linearly related to that of the global ocean carbon storage ($V\delta\overline{C}$), which can then be decomposed into different carbon pump components:

$$\delta\overline{C} = \underbrace{\delta\overline{C_{sat}^T} + \delta\overline{C_{sat}^S}}_{solubility} + \underbrace{\delta\overline{C_{org}}}_{organic} + \underbrace{\delta\overline{C_{CaCO_3}} + \delta\overline{C_{sat}^A}}_{carbonate} + \delta\overline{C_{dis}}. \qquad (2)$$

The first two terms (δC_{sat}^T, δC_{sat}^S) represent the temperature and salinity dependence of the solubility. The second group is the organic pump, measuring the cumulative effect of respiration of organic matter, which is linked to the preformed phosphate, $\delta\overline{C_{org}} = -R_{C:P}\delta\overline{P_{pre}}$. The third group is primarily controlled by the carbonate pump, including the contribution of preformed alkalinity and the cumulative remineralization of $CaCO_3$ particles. The last term is the effect of air-sea disequilibrium in regions of water mass formation, which is then transported into the interior ocean.

Combining Eqs. (1) and (2), changes in atmospheric CO_2 can be attributed to different mechanisms. The constant of proportionality depends on the size of the oceanic and atmospheric carbon reservoir and the global mean buffer factor. As a rule of thumb, $1\mu M$ increase in the ocean carbon storage ($\delta\overline{C}$) leads to approximately 1 ppm decrease in the atmospheric CO_2.

To calculate the individual effects, we follow the methodology of *Ito and Follows* [2013]. The diagnostic calculation is based on the parameters and inventories used in our model. C_{org} is determined based on the Apparent Oxygen Utilization (AOU). This assumes that, when water parcels leave the surface layer, their oxygen content is in equilibrium with the atmospheric oxygen reservoir (often an overestimation of the true dissolved O_2 content of surface waters). Theoretically, preformed alkalinity is also set when the water is last in contact with the mixed layer. In practice, multiple linear regression can be used to estimate the preformed alkalinity for each climate states using salinity and preformed phosphorus as the input parameters. This allows us to calculate the regenerated alkalinity and the carbonate pump, C_{CaCO_3}. Preformed DIC (C_{pre}) is determined by subtracting organic and carbonate pumps (C_{org}, C_{CaCO_3}) from the total DIC. Saturation DIC concentration C_{sat} is calculated from thermodynamic equilibrium relations and depends on temperature, salinity, alkalinity and pCO_2 (although it mainly reflects the temperature of water masses). Finally, the air-sea disequilibrium component C_{dis} is determined as a residual between C_{pre} and C_{sat}. The properties of C_{sat} and C_{dis} are determined at the time of water mass formation, and their distributions correlates with hydrographic structures. Note that the AOU approximation implies a slight overestimation of C_{org} and underestimation of C_{dis}.

Carbon pumps and their changes between the two climate states are shown in Table S1.

Text S4. Discussion of carbon pumps

The reduction of the oceanic carbon storage C_{org} (an atmospheric CO_2 increase of +52 ppm; see Table S1) is associated with a weakening of Antarctic productivity and an increase in the preformed phosphorus of the AABW-like water. As a constant $CaCO_3$ rain ratio is assumed in our model, the carbonate pump C_{CaCO3} weakens along with the organic pump C_{org}, leading to an additional ocean carbon storage due to an increase in the preformed alkalinity. The net effect of the weakened carbonate pump decreases the atmospheric CO_2 by 16 ppm.

If the effect of glacial iron fertilization were to be included in our simulations, the simulated atmospheric pCO_2 may further decrease by a few tens of ppm [*Bopp et al.*, 2003; *Parekh et al.*, 2006]. The reconstruction of preformed nutrient content for the glacial AABW is still elusive [*Francois and et al.*, 1997; *Toggweiler*, 1999; *Sigman et al.*, 2010; *Watson et al.*, 2015]. While the mechanistic link between glacial-interglacial changes in Subantarctic productivity and Antarctic preformed phosphorus is not fully understood, the glacial deep Pacific contained a lower level of dissolved O_2 [*Galbraith et al.*, 2007; *Jaccard et al.*, 2009] indicating that the iron fertilization of the Subantarctic likely influenced the Antarctic preformed phosphate and the amount of regenerated nutrients in deep waters.

In reality the reduction of land biomass likely added approximately 500 PgC to the ocean-atmosphere system during recent glacial periods, leading to an atmospheric CO_2 increase of $\sim$15 ppm [*Sigman and Boyle*, 2000]. Furthermore, the effect of land ice volume raises the mean salinity of the seawater, raising atmospheric CO_2 by about $\sim$7 ppm [*Sigman and Boyle*, 2000]. These effects are not accounted for in our study, and so the transfer of carbon to the deep water has to be the equivalent of about -102 ppm in order to reproduce the observed glacial CO_2 drawdown of -80 ppm.

While the dissolution of carbonate sediment is not resolved in our model, the elevated level of DIC in the bottom water makes it more corrosive to sedimentary $CaCO_3$, and the resultant carbonate dissolution would further decrease the atmospheric CO_2 in the Cold state. Additional CO_2 drawdown is expected due to the effect of increased dust deposition and the $CaCO_3$ compensation triggered by the increased bottom water DIC [*Toggweiler*, 1999].

Table S1. Carbon reservoir changes between the Warm and Cold states of the model[a].

	Solubility		Organic	Carbonate		Disequilibrium	net
	δC_{sat}^{T}	δC_{sat}^{S}	δC_{org}	δC_{CaCO3}	δC_{sat}^{A}	δC_{dis}	
δC, μmol/kg	56.4	-0.1	-50.9	-24.2	39.6	+85.3	+106.1
δCO_2, ppm	-57.8	0.1	52.2	24.8	-40.6	-87.5	-108.8
bias corrected	*-23±8*	”	”	”	”	”	*-71±7*

[a] δC refers to the dissolved inorganic carbon concentration in the ocean, while δCO_2 refers to the mixing ratio of carbon dioxide in the atmosphere. The third line accounts for the effect of a realistic ocean temperature change on δC_{sat}^{T} (see section 4 in the main text). See supplementary Information (section S3) for explanation of the different carbon pumps.

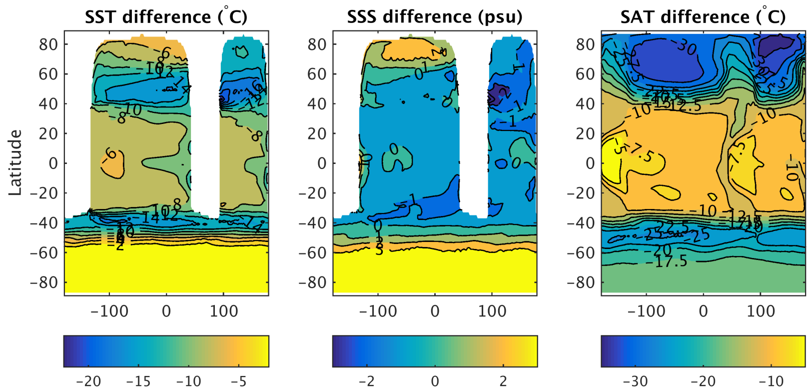

Figure S1. Differences in annual mean Sea Surface Temperature (°C), Sea surface Salinity (psu), and Surface Air Temperature (°C) between the Cold and Warn states. For SST, minimum changes are found in the Southern Hemisphere, south of 60°S, where sea ice is present in both states (the slight cooling in that region is due to a small salinity increase and associated decrease of the freezing point). The pattern of SAT change bares many similarities with that of SST changes. The largest changes in SST and SAT are found in locations that go from ice free conditions in the Warm state to ice covered conditions in the Cold state. The equatorial regions show minima in temperature decrease, notably over the equatorial continents for SAT.

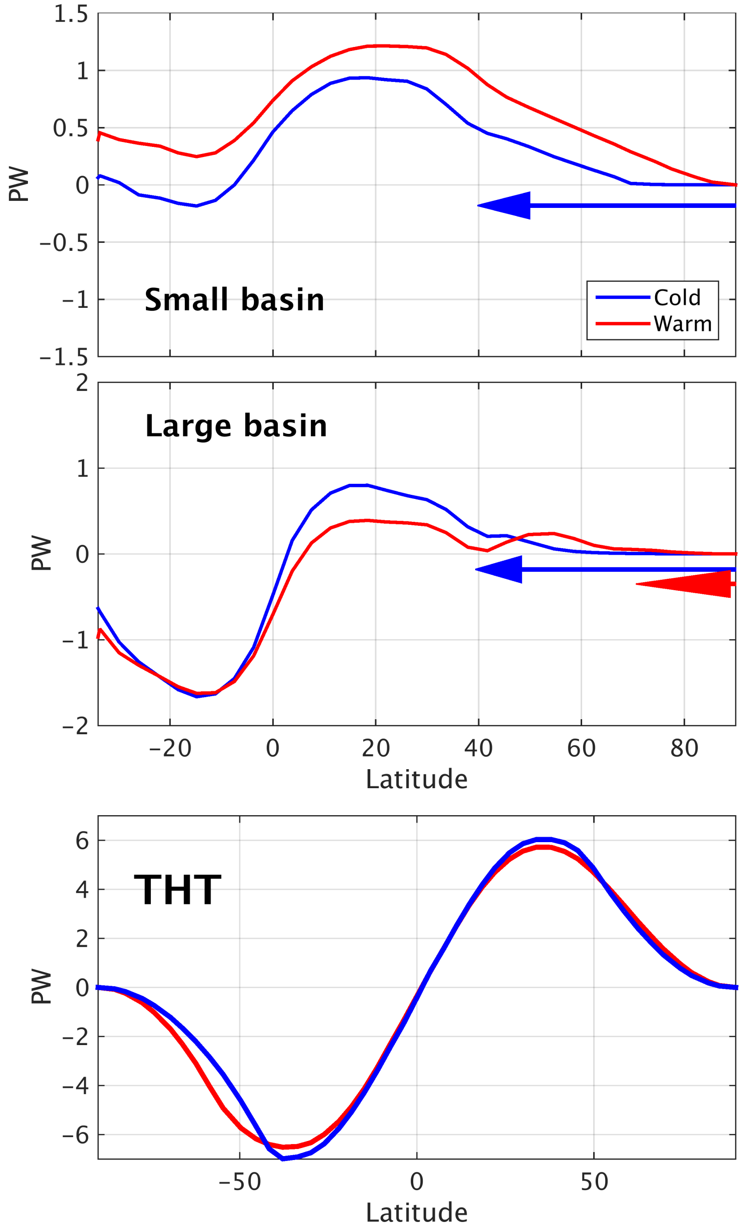

Figure S2. Heat transport (in PW = 10^{15} W) in the Warm (red) and Cold (blue) states: (top) Small basin OHT, (middle) Large Basin OHT, and (bottom) total (ocean plus atmosphere) energy transports. The arrows denote the corresponding sea ice extents. The length of the arrow head indicates the range of the seasonal ice edge.

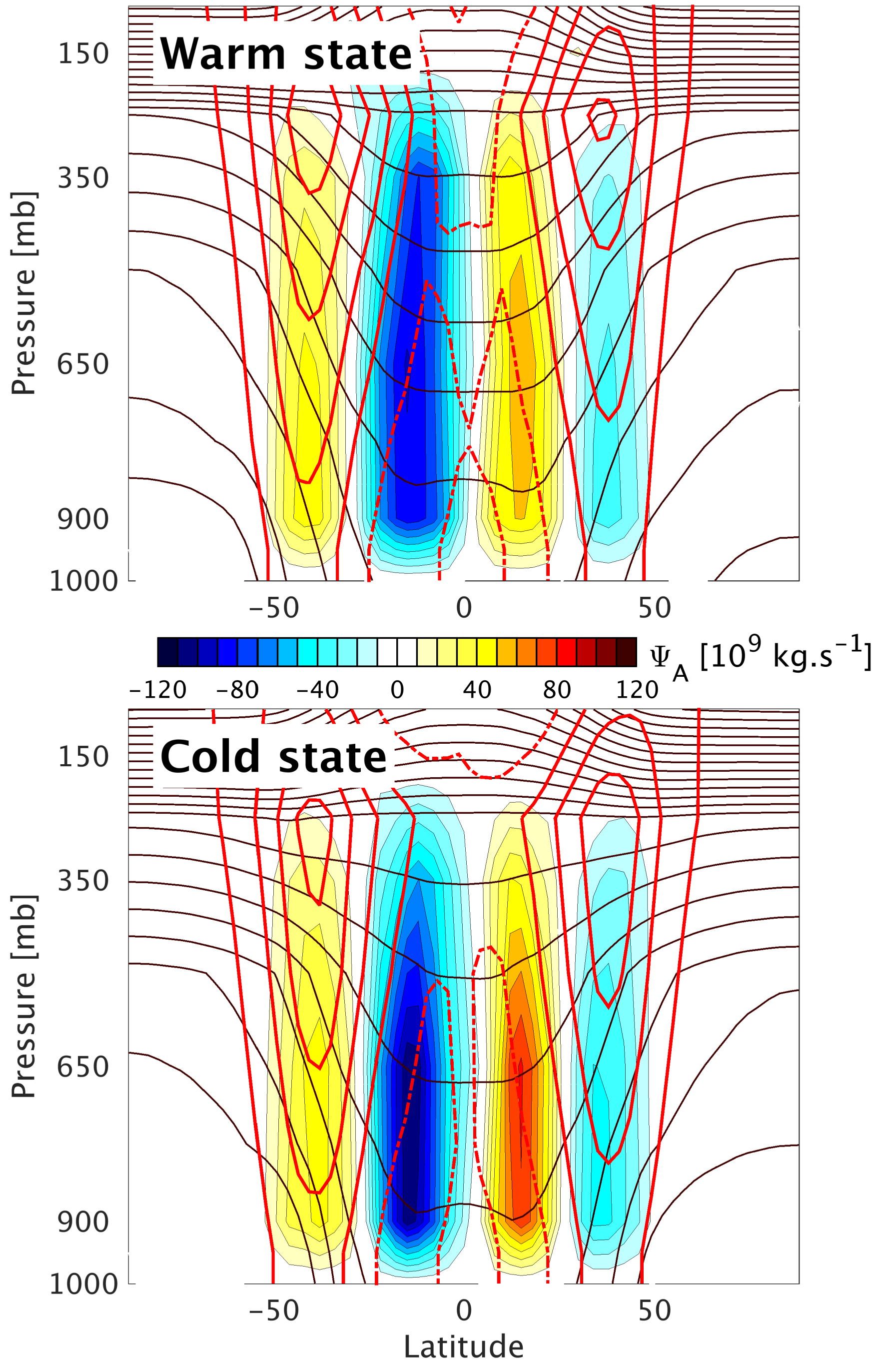

Figure S3. Overturning streamfunction (color shading, contour interval of 10×10^9 kg s^{-1}, the zero contour is omitted), potential temperature (black solid lines with a 10 K contour interval) and zonal-mean zonal winds (red lines, contours at ± 5, ± 15, ± 25 m s^{-1} ..., solid and dashed lines denote westerly and easterly winds, respectively). The Warm state is shown in the top panel and the Cold state in the bottom panel.

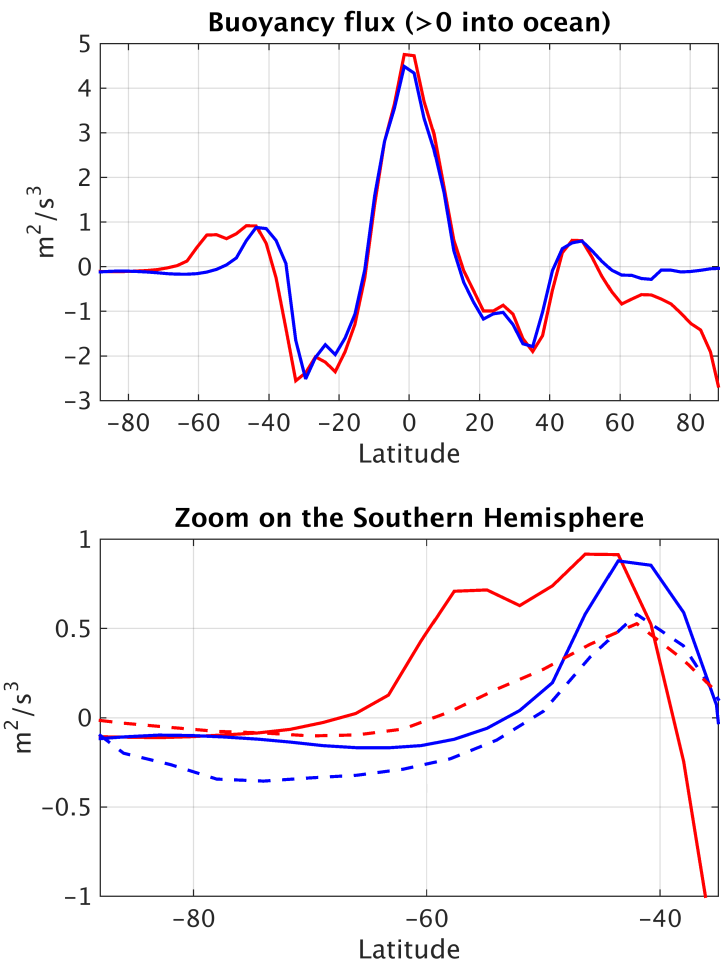

Figure S4. Surface buoyancy fluxes (in m^2 s^{-3}): (top) Annual and zonal mean surface buoyancy fluxes in the Warm (red) and Cold (blue) states, and (bottom) a zoom on the Southern hemisphere between 90 and 45°S. In the bottom panel, the dashed lines shows the profiles of the residual overturning streamfunction (arbitrary units) at 70 m. We observe a northward expansion of the region of buoyancy loss following the expansion of the sea ice cover in the Cold state. This is concomitant with a shift of the zero streamline separating the upper and lower cells as argued by *Ferrari et al.* [2014] and *Watson et al.* [2015]. Unlike in the idealized model of *Nikurashin and Vallis* [2012], the zero flux and zero streamline do not match exactly because of e.g. the time variability of the mixed layer depth [see *Abernathey et al.*, 2011].

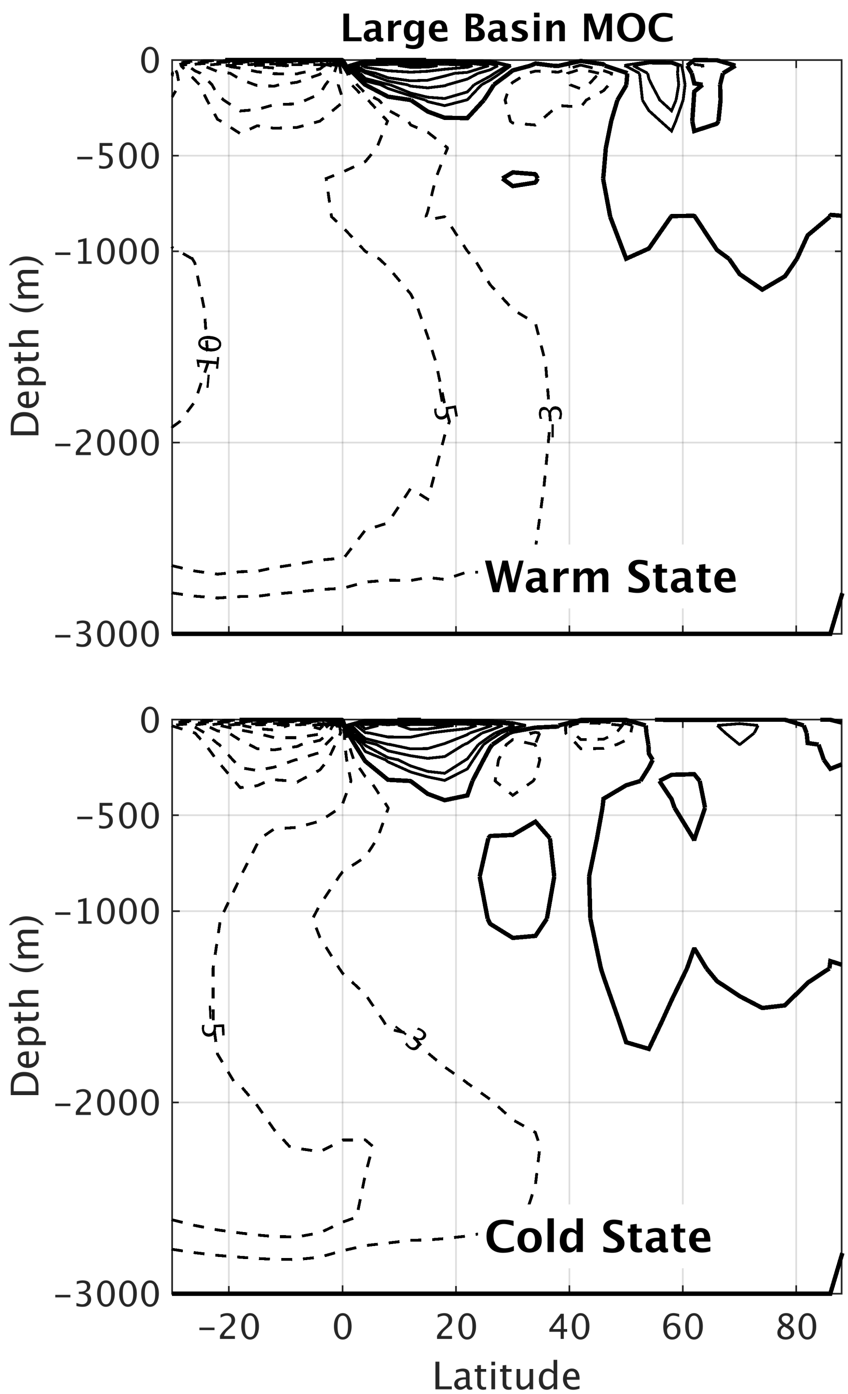

Figure S5. Meridional Overturning Circulation (in Sv) in the Large basin for the Warm state (top) and Cold state (bottom). Solid and dashed lines correspond to clockwise and counter-clockwise circulations, respectively. The zero contour is shown with a thick line.

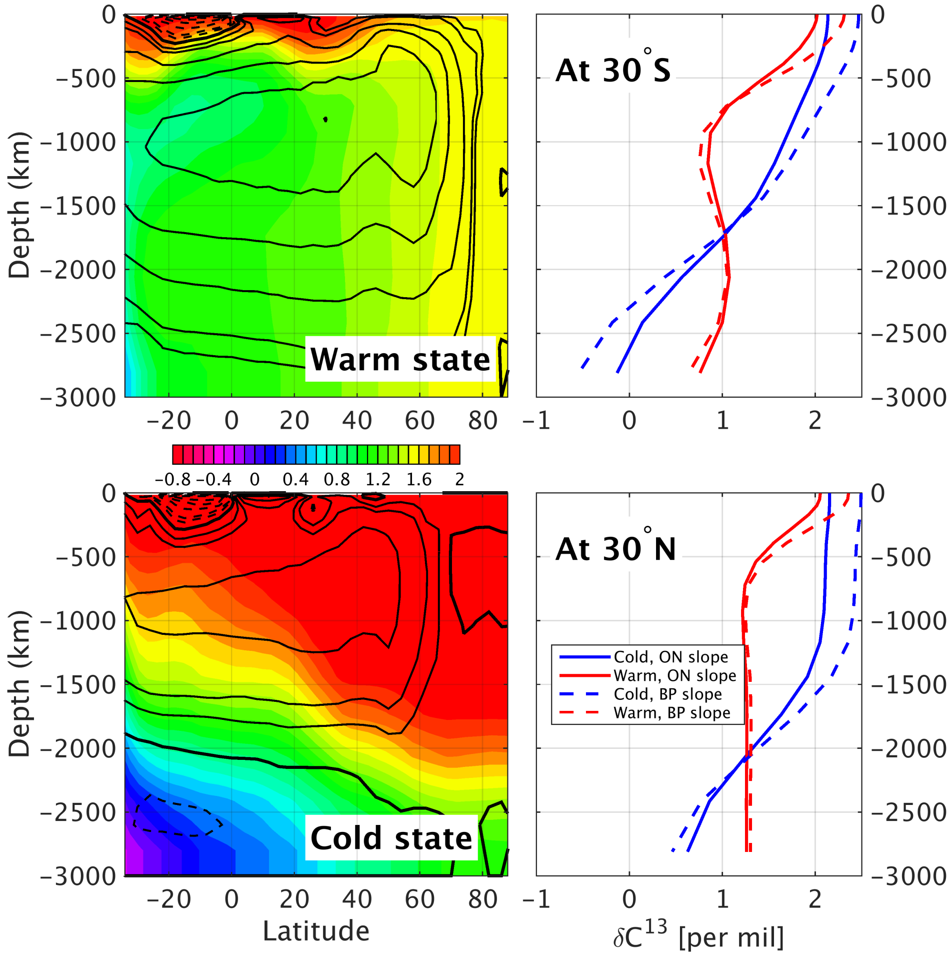

Figure S6. Reconstructed distributions of δC^{13} (in per mil) in the Small basin, estimated from the quasi-linear relationship between phosphate and δC^{13} observed in the present-day ocean. Two linear relationships by *Broecker and Peng* [1982] (BP) and *Olsen and Ninnemann* [2010] (ON) are considered. Note that both estimates correct for the invasion of isotopically-light anthropogenic carbon dioxide. (Left) Depth-latitude distribution of δC^{13} based on the ON relationship for the Warm (top) and Cold (bottom) states. The MOC contours (solid and dashed black) are superimposed. (Right) Vertical profiles at (top) 30°S and (bottom) 30°N highlighting the uncertainties associated with the choice of linear relationship, ON in solid line and BP in dashed lines. Changes in the estimated δC^{13} distribution between the states is much larger than the uncertainties associated with the linear fit. The patterns and magnitude of the reconstructed δC^{13} distributions are in reasonable agreement with those inferred for the present-day ocean and LGM ocean.

References

Abernathey, R., J. Marshall, and D. Ferreira (2011), The dependence of southern ocean meridional overturning on wind stress, *J. Phys. Oceanogr.*, *41*, 2261–2278.

Adcroft, A., and J.-M. Campin (2004), Re-scaled height coordinates for accurate representation of free-surface flows in ocean circulation models, *Ocean Modell.*, *7*, 269–284.

Adcroft, A., J. Campin, C. Hill, and J. Marshall (2004), Implementation of an atmosphere-ocean general circulation model on the expanded spherical cube, *Mon. Wea. Rev.*, *132*, 2845–2863.

Bopp, L., K. E. Kohfeld, C. Le Quéré, and O. Aumont (2003), Dust impact on marine biota and atmospheric co2 during glacial periods, *Paleoceanography*, *18*, 1046.

Broecker, W. S., and T.-H. Peng (1982), *Tracers in the Sea*, Lamont-Doherty Geological Observatory, Columbia University.

Campin, J.-M., J. Marshall, and D. Ferreira (2008), Sea ice-ocean coupling using a rescaled vertical coordinate $z^\star$, *Ocean Modell.*, *24*, 1–14.

Dutkiewicz, S., P. Heimbach, M. J. Follows, and J. C. Marshall (2006), Controls on ocean productivity and air-sea carbon flux: an adjoint model sensitivity study, *Geophys. Res. Lett.*, *33*(2), L02,603.

Enderton, D., and J. Marshall (2009), Explorations of atmosphere-ocean-ice climates on an aqua-planet and their meridional energy transports, *J. Atmos. Sci.*, *66*, 1593–1611.

Ferrari, R., and D. Ferreira (2011), What processes drive the ocean heat transport?, *Ocean Modell.*, *38*, 171–186.

Ferrari, R., M. J. Jansen, J. F. Adkins, A. Butke, A. L. Stewart, and A. F. Thompson (2014), Antarctic sea ice control on ocean circulation in present and glacial climates, *Proc. Natl. Acad. Sci.*, *111*(24), 8753–8758.

Ferreira, D., J. Marshall, and J.-M. Campin (2010), Localization of deep water formation: role of atmospheric moisture transport and geometrical constraints on ocean circulation, *J. Climate*, *23*, 1456–1476.

Ferreira, D., J. Marshall, and B. Rose (2011), Climate determinism revisited: multiple equilibria in a complex climate model, *J. Climate*, *24*, 992–1012.

Francois, R. F., and et al. (1997), Water column stratification in the southern ocean contributed to the lowering of glacial atmospheric co2, *Nature*, *389*, 929–935.

Galbraith, E. D., S. L. Jaccard, T. F. Petersen, D. M. Sigman, G. H. Haugh, M. Cook, J. R. Southon, and R. F. Francois (2007), Carbon dioxide release from the north pacific abyss during the last deglaciation, *Nature*, *449*, 890–893.

Gent, P. R., and J. C. McWilliams (1990), Isopycnic mixing in ocean circulation models, *J. Phys. Oceanogr.*, *20*, 150–155.

Ito, T., and M. J. Follows (2005), Preformed phosphate, soft tissue pump and atmospheric CO_2, *J. Mar. Res.*, *63*, 813–839.

Ito, T., and M. J. Follows (2013), Air-sea disequilibrium of carbon dioxide enhances the biological carbon sequestration in the southern ocean, *Glob. Biogeochem. Cy.*, *27*, 1–10.

Jaccard, S. L., E. D. Galbraith, D. M. Sigman, G. H. Haugh, R. F. Francois, T. F. Petersen, P. Dulski, and H. R. Thierstein (2009), Subarctic pacific evidence for a glacial deepening of the oceanic respired carbon pool, *Earth and Planet. Sci. Lett.*, *277*, 156–165.

Klinger, B. A., J. Marshall, and U. Send (1996), Representation of convective plumes by vertical adjustment, *J. Geophys. Res.*, *C8*(101), 18,175–18,182.

Marshall, J., A. Adcroft, C. Hill, L. Perelman, and C. Heisey (1997a), A finite-volume, incompressible navier stokes model for studies of the ocean on parallel computers, *J. Geophys. Res.*, *102*(C3), 5753–5766.

Marshall, J., C. Hill, L. Perelman, and A. Adcroft (1997b), Hydrostatic, quasi-hydrostatic, and nonhydrostatic ocean modeling, *J. Geophys. Res.*, *102*(C3), 5733–5752.

Marshall, J., A. Adcroft, J.-M. Campin, C. Hill, and A. White (2004), Atmosphere-ocean modeling exploiting fluid isomorphisms, *Mon. Wea. Rev.*, *132*, 2882–2894.

Marshall, J., D. Ferreira, J. Campin, and D. Enderton (2007), Mean climate and variability of the atmosphere and ocean on an aquaplanet, *J. Atmos. Sci.*, *64*, 4270–4286.

Molteni, F. (2003), Atmospheric simulations using a GCM with simplified physical parametrizations. I: model climatology and variability in multi-decadal experiments., *Climate Dyn.*, *64*, 175–191.

Nikurashin, M., and G. K. Vallis (2012), A theory of the interhemispheric meridional overturning circulation and associated stratification, *J. Phys. Oceanogr.*, *42*(10), 1652–1667, doi:10.1175/JPO-D-11-0189.1.

Olsen, A., and U. Ninnemann (2010), Large δ^{13}C gradients in the preindustrial north atlantic revealed, *Science*, *330*, 658–659.

Parekh, P., S. Dutkiewicz, M. J. Follows, and T. Ito (2006), Atmospheric carbon dioxide in a less dusty world, *Geophys. Res. Lett.*, *33*, L03,610.

Pohl, A., Y.Donnadieu, G. L. Hir, and D. Ferreira (2017), The climatic significance of late ordovician-early silurian black shales, *Paleoceanography*, *Submitted*.

Redi, M. H. (1982), Oceanic isopycnal mixing by coordinate rotation, *J. Phys. Oceanogr.*, *12*, 1154–1158.

Sigman, D. M., and E. A. Boyle (2000), Glacial/interglacial variations in atmospheric carbon dioxide, *Nature*, *407*, 859–869.

Sigman, D. M., M. P. Hain, and G. H. Haugh (2010), The polar ocean and glacial cycles in atmospheric co2 concentration, *Nature*, *466*, 47–55.

Stone, P. H. (1978), Constraints on dynamical transports of energy on a spherical planet, *Dyn. Atmos. Oceans*, *2*, 123–139.

Toggweiler, J. R. (1999), Variations in atmospheric co2 driven by ventilation of the ocean's deepest water, *Paleoceanography*, *14*, 571–588.

Watson, A. J., G. K. Vallis, and M. Nikurashin (2015), Southern ocean buoyancy forcing of ocean ventilation and glacial atmospheric CO_2, *Nature Geoscience*, *8*, 861–864.

Winton, M. (2000), A reformulated three-layer sea ice model, *J. Atmos. Oceanic Technol.*, *17*, 525–531.